Boundary-volume Lippmann Schwinger formulation and fast iteration schemes for numerical homogenization of conductive composites. Cases of arbitrary contrasts and Kapitza interface

Quy-Dong To, Guy Bonnet

Boundary-volume Lippmann Schwinger formulation and fast iteration schemes for numerical homogenization of conductive composites. Cases of arbitrary contrasts and Kapitza interface.

Quy-Dong To[a,*], Guy Bonnet[a]

[a]*Laboratoire MSME, Univ Gustave Eiffel, CNRS UMR 8208, F-77454 Marne-la-Vallée, France*

Abstract

In this paper, we present a boundary-volume based Lippmann Schwinger integral equation for numerical homogenization problems of heterogeneous conductive materials with arbitrary contrast ratio and imperfect interface behavior. It is shown that the interior temperature gradient within each homogeneous phase is connected to the material dissimilarity quantities at all boundaries between different phases. The Kapitza interface model can also be included in the formulation. The basic FFT iteration schemes converge fast even for infinite contrast in the case of usual interface conditions. In the case of Kapitza's interface, Conjugate Gradient schemes based on the new formulation converge fast and yield accurate results when compared with standard Finite Element Method.

Keywords: Fast Fourier Transform, Numerical homogenization method, Infinite contrast, Kapitza resistance model

*Corresponding author. Email: quy-dong.to@univ-eiffel.fr

1. Introduction

Among the numerical homogenization methods in material science, Fast Fourier Transform based methods have seen a rapid development during the last decade and have been recognized as an efficient alternative to the traditional finite element method. Given a boundary value problem in the unit cell, the Lippmann Schwinger (LS) type integral equations (Brown Jr, 1955; Kröner, 1977) is first derived and the iterative resolution schemes are then employed to obtain the solution. The robust Fourier Transform algorithm is used to switch between the Fourier and the physical space and evaluate efficiently the mathematical operations in Fourier space, e.g convolution integrals involving the Green functions. The method works on regular grids, which is compatible with tomography image and does not require the assembly of stiffness matrices like the Finite Element Method.

The first papers that included those elements and established the FFT numerical homogenization method can be traced back to (Moulinec and Suquet, 1994; Michel et al., 1999) in the context of elasticity. They used a basic form of iterative scheme which is subject to limitations, especially slow convergence at high contrast ratio. To improve the performance, the accelerated scheme (Eyre and Milton, 1999; Monchiet and Bonnet, 2012) and augmented Lagrange scheme (Michel et al., 2001) were proposed. The Newton-Krylov solvers can be also used as an efficient resolution method (Zeman et al., 2010; Vondřejc et al., 2014; Schneider, 2019; Kabel et al., 2014; Brisard and Dormieux, 2010) for LS equations. As shown by (Moulinec and Silva, 2014), all the iterative schemes have convergence issues at the infinite contrast, specifically they fail to match the demanding criteria on the stress equilibrium condition. Willot et al. (2014) used a finite difference scheme leading to a modified expression of Green tensors, that improves the results for infinite contrast cases. In the case of porous materials, a technique is to eliminate the void field which is not unique and establish the new LS equations for

the skeleton field (To and Bonnet, 2020; To et al., 2021). The basic iteration scheme (i.e. scheme equivalent to the Neumann series) of the latter converges fast even with the demanding convergence criteria. Recently, Schneider (2020) suggested that the ill convergent behavior for porous material of Michel-Moulinec related schemes can be avoided using alternative discretizations.

In addition to infinite contrast issue, composite materials can have a specific behavior between two different phases that involve a discontinuity at the interface of some local fields (displacement, temperature,...). A recent work by Monchiet (2018) studied this problem in the context of FFT solvers. However, the technique used by the latter relies on interpolation functions in each subdomain and renders the methods rather difficult in practice. A simpler technique is to use a boundary source term to enforce the Dirichlet or Kapitza boundary conditions (To et al., 2021; To and Bonnet, 2023a) with a penalty coefficient. In the case of composites, we can see that this technique can be employed at the interface between two different phases.

In the present paper and in the context of conductive materials, we extend our recent results on porous materials (To and Bonnet, 2020; To et al., 2021) to the case of composites with arbitrary contrast, including both pore and infinite conductive phase. With suitable treatment of discontinuities and singularities, we obtain a LS integral equation where the interior gradient field is connected to the material mismatch quantities on the interface boundary (i.e. boundary-volume based LS integral equation). As a result, the Kapitza interface model can be included naturally and in a relatively simple way. Furthermore, we find that the basic iteration scheme converges fast for classical interface continuity condition (even for infinite contrast) and BICGSTAB scheme associated to the integral equations in the case of Kapitza interface has a fast convergent behavior. The paper is organized as follows. After the

Introduction and the mathematical notions of Fourier Transform, Section 3 is devoted to the derivation of boundary based LS equations for composites with perfect and imperfect interface. Section 4 presents numerical applications and convergence studies. Finally, the conclusions are presented in the last section.

2. Mathematical foundation and notations

The bold characters $\boldsymbol{A}, \boldsymbol{u}$ is used for tensorial quantities and normal characters φ, θ for scalars. The notation $\boldsymbol{u} \otimes \boldsymbol{v}$ stands for tensorial products and $\boldsymbol{uv}$ for dot products between two tensor quantities $\boldsymbol{u}$ and $\boldsymbol{v}$. The notation $\boldsymbol{A} * \boldsymbol{u}$ represents convolution product and will be explained later.

2.1. Fourier transform and Green operators

We shall limit this work to periodic functions that admit Fourier series expansions. A $V-$ periodic function $\boldsymbol{u}(\boldsymbol{x})$ of Cartesian coordinates $\boldsymbol{x}(x_1, x_2, x_3)$ can be expressed as Fourier series

$$\boldsymbol{u}(\boldsymbol{x}) = \sum_{\boldsymbol{\xi}} \widehat{\boldsymbol{u}}(\boldsymbol{\xi}) e^{i\boldsymbol{\xi}\boldsymbol{x}}, \tag{1}$$

where $\widehat{\boldsymbol{u}}(\boldsymbol{\xi})$ is the Fourier transform of $\boldsymbol{u}(\boldsymbol{x})$

$$\widehat{\boldsymbol{u}}(\boldsymbol{\xi}) = \mathcal{F}[\boldsymbol{u}(\boldsymbol{x})] = \frac{1}{V} \int_V \boldsymbol{u}(\boldsymbol{x}) e^{-i\boldsymbol{\xi}\boldsymbol{x}} d\boldsymbol{x}, \quad i = \sqrt{-1}, \tag{2}$$

and $\boldsymbol{\xi}(\xi_1, \xi_2, \xi_3)$ the wave vector

$$\xi_k = 2\pi n_k / L_k, \quad n_k = 0, \pm 1, \pm 2, ..., \pm\infty, \quad k = 1, 2, 3 \tag{3}$$

and L_1, L_2, L_3 being the dimensions of the period V along directions x_1, x_2, x_3.

The convolution product $*$ of operator $\boldsymbol{A}$ on $\boldsymbol{u}$ can be expressed as

$$\boldsymbol{A}(\boldsymbol{x}) * \boldsymbol{u}(\boldsymbol{x}) = \sum_{\boldsymbol{\xi}} \widehat{\boldsymbol{A}}(\boldsymbol{\xi})\widehat{\boldsymbol{u}}(\boldsymbol{\xi})e^{i\boldsymbol{\xi}\boldsymbol{x}} \tag{4}$$

and the normal product has the following form

$$\boldsymbol{A}(\boldsymbol{x})\boldsymbol{u}(\boldsymbol{x}) = \sum_{\boldsymbol{\xi}} [\widehat{\boldsymbol{A}}(\boldsymbol{\xi}) * \widehat{\boldsymbol{u}}(\boldsymbol{\xi})]e^{i\boldsymbol{\xi}\boldsymbol{x}} \tag{5}$$

with

$$\widehat{\boldsymbol{A}}(\boldsymbol{\xi}) * \widehat{\boldsymbol{u}}(\boldsymbol{\xi}) = \sum_{\boldsymbol{\xi}'} \widehat{\boldsymbol{A}}(\boldsymbol{\xi} - \boldsymbol{\xi}')\widehat{\boldsymbol{u}}(\boldsymbol{\xi}') \tag{6}$$

In the paper, we use a set of Green tensors $\boldsymbol{P}$, $\boldsymbol{R}$ and S whose expressions in the Fourier space $\widehat{\boldsymbol{P}}(\boldsymbol{\xi})$, $\widehat{\boldsymbol{R}}(\boldsymbol{\xi})$ and $\widehat{S}(\boldsymbol{\xi})$ are explicit functions of wavevector $\boldsymbol{\xi}$

$$\widehat{\boldsymbol{P}}(\boldsymbol{\xi}) = \frac{\boldsymbol{\xi} \otimes \boldsymbol{\xi}}{\xi^2}, \quad \widehat{\boldsymbol{R}}(\boldsymbol{\xi}) = \frac{i\boldsymbol{\xi}}{\xi^2}, \quad \widehat{S}(\boldsymbol{\xi}) = \frac{1}{\xi^2}, \quad \xi = \|\boldsymbol{\xi}\| \tag{7}$$

and null for $\boldsymbol{\xi} = \boldsymbol{0}$

$$\widehat{\boldsymbol{P}}(\boldsymbol{0}) = \boldsymbol{0}, \quad \widehat{\boldsymbol{R}}(\boldsymbol{0}) = \boldsymbol{0}, \quad \widehat{S}(\boldsymbol{0}) = 0 \tag{8}$$

Operator $\boldsymbol{R}$ has the following property

$$-\boldsymbol{R} * \nabla\varphi = \varphi - \langle\varphi\rangle \tag{9}$$

for all function φ with average $\langle\varphi\rangle$

$$\langle\varphi\rangle = \frac{1}{V}\int_V \varphi d\boldsymbol{x} \tag{10}$$

2.2. Characteristic functions, gradients and delta function of a surface

Let us imagine that a characteristic function χ associated to volume Ω is defined by

$$\chi(\boldsymbol{x}) = 1 \quad \text{in } \Omega, \quad \chi(\boldsymbol{x}) = 0 \quad \text{in } V \backslash \Omega. \tag{11}$$

The Fourier transforms of the characteristics functions χ, called the form factor, is

$$\widehat{\chi}(\boldsymbol{\xi}) = \frac{1}{V} \int_{\Omega} e^{-i\boldsymbol{\xi}\boldsymbol{x}} d\boldsymbol{x}. \tag{12}$$

Taking gradient of the characteristic function yields surface delta function

$$\nabla \chi(\boldsymbol{x}) = -(\boldsymbol{n}\delta)_{\Gamma}(\boldsymbol{x}) \tag{13}$$

where $\boldsymbol{n}$ is the outward normal vector on the boundary Γ of Ω and δ the delta distribution associated to Γ. The delta based distribution family $\delta_{\Gamma}(\boldsymbol{x})$, $(\boldsymbol{n}\delta)_{\Gamma}(\boldsymbol{x})$ and $(\boldsymbol{n} \otimes \boldsymbol{n}\delta)_{\Gamma}(\boldsymbol{x})$ can be defined on any open or close surface Γ. They belong to the class of distribution $f(\boldsymbol{x})\delta_{\Gamma}(\boldsymbol{x})$ with $f(\boldsymbol{x})$ being the continuous strength function defined on Γ, admitting the Fourier transforms

$$\widehat{f\delta_{\Gamma}}(\boldsymbol{\xi}) = \frac{1}{V} \int_{\Gamma} f(\boldsymbol{x}) e^{-i\boldsymbol{\xi}\boldsymbol{x}} d\boldsymbol{x} \tag{14}$$

The Fourier transforms of the distributions $\delta_{\Gamma}(\boldsymbol{x})$, $(\boldsymbol{n}\delta)_{\Gamma}(\boldsymbol{x})$ and $(\boldsymbol{n}\otimes\boldsymbol{n}\delta)_{\Gamma}(\boldsymbol{x})$ for some 2D geometries like circles and lines are given in Appendix A. Since any 2D curve Γ can be discretized into a set of polylines $\mathcal{L}_i$, the analytical expressions for 2D subjects can be done by superposing expressions of each $\mathcal{L}_i$

$$\widehat{f\delta_{\Gamma}}(\boldsymbol{\xi}) = \sum_i \widehat{f\delta_{\mathcal{L}_i}}(\boldsymbol{\xi}), \quad \Gamma = \bigcup_i \mathcal{L}_i \tag{15}$$

The same rule can be applied to any 3D surfaces which can be approximated as union of planar polygonal surfaces whose form factors are also known (To and Bonnet, 2023b). Pixel and voxel based boundaries also belong to the same category as they are collections of linear segments or plane quadrilaterals surfaces (To and Bonnet, 2020).

Let us consider a function φ defined on V that is continuous from both sides of Γ but may be discontinuous on Γ. With φ admitting the Fourier representation (1), we have the relation

$$\varphi = \frac{1}{2}(\varphi^+ + \varphi^-) \quad \text{on } \Gamma \tag{16}$$

where φ^+ and φ^- are the limits of the function φ from two sides of the surface. This relation is an extension of the theorem of Dirichlet on Fourier series which states that at a discontinuity, the Fourier series converges to such a middle value (see also Taylor, 2001, for the case of multivariate functions in $L^1(\mathbb{R}^n)$[1]). Consequently, the following results involving the product of discontinuous function and a delta based distribution can be obtained

$$(f\delta_\Gamma)\varphi = \frac{1}{2}(\varphi^+ + \varphi^-)(f\delta_\Gamma) \tag{17}$$

If the Fourier transform of the delta distribution $f\delta$ and a function φ are known, the Fourier transform of their product can be evaluated by (6) as

$$[f\delta_\Gamma\varphi](\boldsymbol{\xi}) = \widehat{f\delta_\Gamma}(\boldsymbol{\xi}) * \widehat{\varphi}(\boldsymbol{\xi}) = \sum_{\boldsymbol{\xi}'} \widehat{f\delta_\Gamma}(\boldsymbol{\xi} - \boldsymbol{\xi}')\widehat{\varphi}(\boldsymbol{\xi}') \tag{18}$$

[1]In the case of N dimensions, the series Fourier point-wise converges to the volume average of φ in an infinitesimal sphere centered at the point of interest.

3. Boundary-volume Lippmann Schwinger formulation for composites

3.1. Integral equations for homogeneous phase and for periodic heterogeneous materials

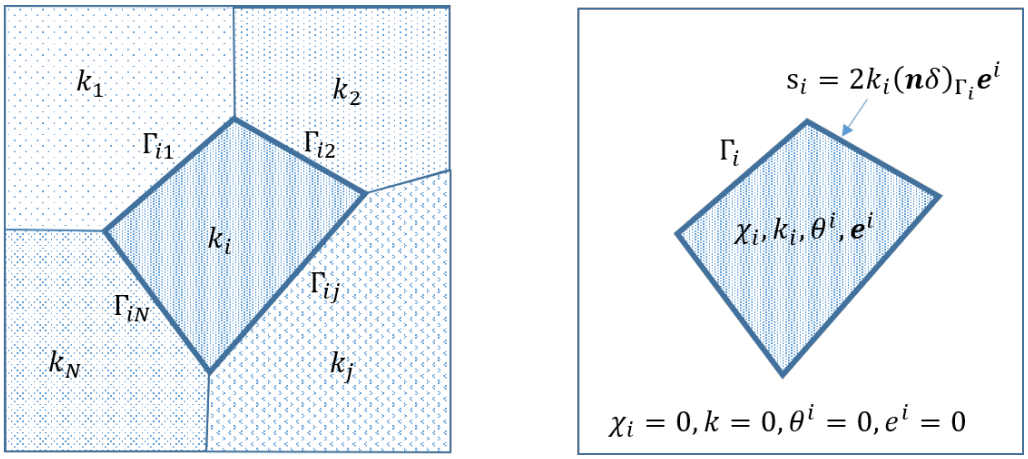

Figure 1: Sketch of composites material. Left: Phases in composites material and boundary. Right: Problem involving phase i surrounded by void

Let us start with problems for a material whose conductivity $k(\boldsymbol{x})$ depends on coordinate $\boldsymbol{x}$ and is V periodic (see Fig. 1). The material is composed of N phases and in each phase i of volume Ω_i boundary Γ_i, the material is homogeneous and isotropic, characterized by a characteristic function χ_i and conductivity k_i

$$\chi_i(\boldsymbol{x}) = 1 \quad \text{in } \Omega_i, \quad \chi_i(\boldsymbol{x}) = 0 \quad \text{in } V \backslash \Omega_i \tag{19}$$

and

$$k(\boldsymbol{x}) = \sum_{i=1}^{N} k_i \chi_i(\boldsymbol{x}), \quad \sum_{i=1}^{N} \chi_i(\boldsymbol{x}) = 1 \quad \forall \boldsymbol{x} \tag{20}$$

To solve the local problem, let us define the (minus) temperature gradient

terms $\boldsymbol{e}$ and (periodic) temperature fluctuation θ as follows

$$\boldsymbol{e} = \boldsymbol{E} + \nabla\theta \tag{21}$$

where $\boldsymbol{E}$ is the volume average of $\boldsymbol{e}$. From now on, we shall refer θ shortly to temperature for convenient reason. To ensure the energy conservation of the heat flux $j(\boldsymbol{x}) = k(\boldsymbol{x})\boldsymbol{e}$ and div$\boldsymbol{j} = 0$, θ must satisfy the governing equation:

$$\boldsymbol{R} * k(\nabla\theta + \boldsymbol{E}) = 0 \tag{22}$$

Due to the gradient $\nabla\theta$ in Eqs. 21,22, θ is defined up to a constant. We can set in advance its average $\Theta = \langle\theta\rangle$ as being any constant, for example $\Theta = 0$, without affecting the solution $\boldsymbol{e}$ of the cell problem.

Instead of considering the conservation equation for the whole heterogeneous media, we establish the equation related to each phase i. To do that, we consider that each phase i is surrounded by void and add the exchange with the surrounding material via a source term s_i localized on Γ_i. The governing equation can be decomposed into N equations by introducing the source Green's tensor S as in (To et al., 2021) to account for the source effect :

$$\boldsymbol{R} * k_i\chi_i(\nabla\theta + \boldsymbol{E}) + S * s_i = 0, \quad \forall i = 1, 2, .., N \tag{23}$$

We denote $\boldsymbol{e}^i$ and θ^i the gradient and temperature solution in phase i and vanishing outside that phase, so that:

$$\theta^i = \chi_i\theta, \quad \boldsymbol{e}^i = \chi_i\boldsymbol{e} = \chi_i(\boldsymbol{E} + \nabla\theta) \tag{24}$$

with the relation (To and Bonnet, 2020)

$$\boldsymbol{e}^i = \boldsymbol{E}\chi_i + \nabla(\chi_i\theta) - \theta\nabla\chi_i = \boldsymbol{E}\chi_i + \nabla\theta^i + 2(\boldsymbol{n}\delta)_{\Gamma_i}\theta^i \tag{25}$$

We note that as θ^i is zero outside Γ^i, and thus $(\boldsymbol{n}\delta)_{\Gamma_i}\theta = 2(\boldsymbol{n}\delta)_{\Gamma_i}\theta^i$ by (17) and thus discontinuous on Γ_i. As we can see $\nabla\theta^i$ is expected to have a delta Dirac distribution associated to Γ_i. In this case, $\boldsymbol{e}^i$ only keeps the regular part of $\nabla\theta^i$ as the Dirac term $2(\boldsymbol{n}\delta)_{\Gamma_i}\theta^i$ cancels the singularity of $\nabla\theta^i$.

Additionally, we also exploit the fact that due to the heat flux at the boundary equal to $k_i\boldsymbol{e}^i$ and vanishing in the void (outside Γ_i), applying (17), the source term s_i is given by (see To et al., 2021, for more details)

$$s_i = 2k_i(\boldsymbol{n}\delta)_{\Gamma_i}\boldsymbol{e}^i \tag{26}$$

The temperature θ^i of phase i as a function of boundary values at Γ_i of temperature and gradient can be obtained by replacing s_i and $\boldsymbol{e}^i$ by their expressions into (23) and using (9)

$$\theta^i = \Theta^i + \boldsymbol{R} * (\boldsymbol{E}\chi_i + 2(\boldsymbol{n}\delta)_{\Gamma_i}\theta^i) + 2S * (\boldsymbol{n}\delta)_{\Gamma_i}\boldsymbol{e}^i \tag{27}$$

As we can see, the interior temperature depends on the values of temperature $(\boldsymbol{n}\delta)_{\Gamma_i}\theta^i$ and normal gradient $(\boldsymbol{n}\delta)_{\Gamma_i}\boldsymbol{e}^i$ on the boundary. It has the same structure as the classical integral representation used in the context of the Boundary Element Method (Bonnet, 1999) (i.e. computation of the temperature at interior points from surface temperature and gradient) but in the case of periodic problems (see discussion in To et al., 2021). Its expression uses also a constant Θ^i, which is the average of θ^i, $\Theta^i = \langle\theta^i\rangle$. Furthermore this relation is independent of the conductivity k_i of the material within Γ_i. It means that the interior temperature θ^i corresponding to those boundary values is unique, even when phase i is a pore $k_i \to 0$ or a superconductive material $k_i \to \infty$.

Different from Θ which can be set as any constant in advance, say $\Theta = 0$ so that θ is an average free quantity, Θ^i can not be set arbitrarily. Once Θ is

set, the solution θ is expected to be unique (except for void interior points) and as $\theta = \theta^i$ in each phase i, θ^i and Θ^i is also unique. In other words, the solution θ^i, Θ^i in each phases are connected, for example by continuity at the interface and constitute the whole field θ, Θ.

Summing back on all phases i as $\sum_i \theta^i = \theta$, $\sum_i \Theta^i = \Theta$ and $\sum_i \chi_i = 1$, we can derive the global temperature field θ of the composite material

$$\theta = \Theta + 2\boldsymbol{R} * \sum_i (\boldsymbol{n}\delta)_{\Gamma_i} \theta^i + 2S * \sum_i (\boldsymbol{n}\delta)_{\Gamma_i} \boldsymbol{e}^i \tag{28}$$

Next, taking gradient of θ by (21), $\boldsymbol{e}$ can be obtained

$$\boldsymbol{e} = \boldsymbol{E} - 2\boldsymbol{P} * \sum_i (\boldsymbol{n}\delta)_{\Gamma_i} \theta^i + 2\boldsymbol{R} * \sum_i (\boldsymbol{n}\delta)_{\Gamma_i} \boldsymbol{e}^i \tag{29}$$

3.2. Case of perfect interface

The boundary of each phase Γ_i is decomposed into the interface Γ_{ij} between two phases i and j which is

$$\Gamma_i = \bigcup_j \Gamma_{ij}. \tag{30}$$

We assume that the interface Γ_{ij} is perfect, i.e the temperature and normal flux are continuous across this interface.

Applying the decomposition (30) to $\sum_i (\boldsymbol{n}\delta)_{\Gamma_i} \theta^i$ yields

$$\begin{aligned} &\sum_i (\boldsymbol{n}\delta)_{\Gamma_i} \theta^i = \sum_{(i,j)} [(\boldsymbol{n}\delta)_{\Gamma_{ij}} \theta^i + (\boldsymbol{n}\delta)_{\Gamma_{ji}} \theta^j] = \\ &= \sum_{(i,j)} (\boldsymbol{n}\delta)_{\Gamma_{ij}} (\theta^i - \theta^j) = 0. \end{aligned} \tag{31}$$

This identity is due to the fact that the normal vector of Γ_{ij} has the opposite direction of Γ_{ji}, i.e $(\boldsymbol{n}\delta)_{\Gamma_{ij}} = -(\boldsymbol{n}\delta)_{\Gamma_{ji}}$ and the temperature at the interface Γ_{ij} is continuous $\theta^i = \theta^j$ on Γ_{ij}. As a notation, $\sum_i$ represents the sum over all phases i and $\sum_{(i,j)}$ the sum over all phase combination (i, j) which share the common interface Γ_{ij}.

Applying also the decomposition (30) to $\sum_i (\boldsymbol{n}\delta)_{\Gamma_i} \boldsymbol{e}^i$ yields

$$\boldsymbol{e} = \boldsymbol{E} + 2\boldsymbol{R} * \sum_{(i,j)} (\boldsymbol{n}\delta)_{\Gamma_{ij}} (\boldsymbol{e}^i - \boldsymbol{e}^j). \tag{32}$$

In the next step, we shall derive the relation between $\sum_{(i,j)} (\boldsymbol{n}\delta)_{\Gamma_{ij}} (\boldsymbol{e}^i - \boldsymbol{e}^j)$ and $\boldsymbol{e}$ so that we can obtain a governing integral equation on $\boldsymbol{e}$ only.

Since $\boldsymbol{e} = \sum_i \boldsymbol{e}^i$ is equal to $\boldsymbol{e}^i$ and $\boldsymbol{e}^j$ at each side of Γ_{ij}, the relation

$$(\boldsymbol{n}\delta)_{\Gamma_{ij}} \boldsymbol{e} = (\boldsymbol{n}\delta)_{\Gamma_{ij}} (\boldsymbol{e}^i + \boldsymbol{e}^j) \tag{33}$$

must hold. Due to the continuity of flux at Γ_{ij}, we also have

$$k_i (\boldsymbol{n}\delta)_{\Gamma_{ij}} \boldsymbol{e}^i = k_j (\boldsymbol{n}\delta)_{\Gamma_{ij}} \boldsymbol{e}^j. \tag{34}$$

Combining (33) and (34), it is possible to show that

$$(\boldsymbol{n}\delta)_{\Gamma_{ij}} (\boldsymbol{e}^i - \boldsymbol{e}^j) = -\frac{k_i - k_j}{k_i + k_j} (\boldsymbol{n}\delta)_{\Gamma_{ij}} \boldsymbol{e} \tag{35}$$

As we can see $\frac{k_i - k_j}{k_i + k_j}$ is a material mismatch coefficient, playing a role similar to the Dundurs coefficients in elasticity. Substituting (35) into (32) yields

$$\boldsymbol{e} = \boldsymbol{E} - 2\boldsymbol{R} * \sum_{(i,j)} \frac{k_i - k_j}{k_i + k_j} (\boldsymbol{n}\delta)_{\Gamma_{ij}} \boldsymbol{e} \tag{36}$$

or in a more tractable form

$$\boldsymbol{e}(\boldsymbol{x}) = \boldsymbol{E} - 2\sum_{(i,j)} \frac{k_i - k_j}{k_i + k_j} \int_{\Gamma_{ij}} \boldsymbol{R}(\boldsymbol{x} - \boldsymbol{y})[\boldsymbol{e}(\boldsymbol{y})\boldsymbol{n}(\boldsymbol{y})]d\boldsymbol{y} \quad \forall \boldsymbol{x} \in V \tag{37}$$

This is the Fredholm integral equation for $\boldsymbol{e}$ which shows the relation between the interior value of $\boldsymbol{e}$ and the boundary value $\boldsymbol{e}$ via the term $(\boldsymbol{n}\delta)_{\Gamma_{ij}}\boldsymbol{e}$. The equation has some similarities with the Boundary Integral Equation obtained in Greengard and Moura (1994) using the Green function for infinite medium, where the same mismatch coefficients do appear.

If the problem is well posed so that the boundary value exists uniquely, then the whole solution exists uniquely. Even in the case of simply connected voids, $\boldsymbol{e}$ exists uniquely as it is the unique harmonic continuation in the void phase that matches the boundary value via eq. (27).

3.3. Implementation of Kapitza interface model

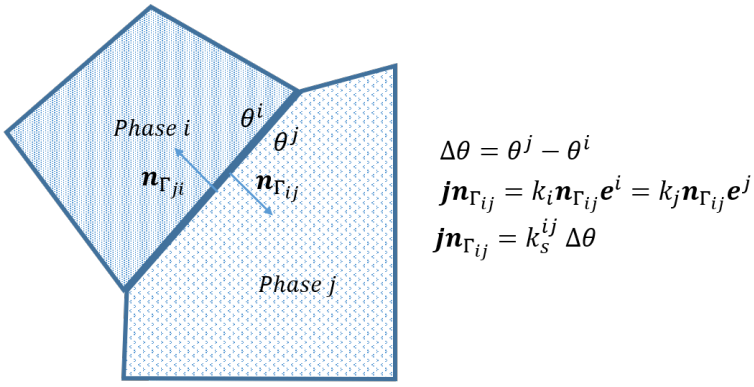

Figure 2: Kapitza interface model between phase i and j

Now let us assume that the interface is not perfect, the temperature field being discontinuous at the boundary of each phase Γ_i, the normal flux being continuous. In this case, $\boldsymbol{e}$ exhibits a Dirac singularity at Γ_i and is no longer equal to the sum of $\boldsymbol{e}^i$. Indeed, summing all the phases i in (25) and

combining (21) yields

$$\widetilde{\boldsymbol{e}} = \boldsymbol{e} + 2\sum_i (\boldsymbol{n}\delta)_{\Gamma_i}\theta^i, \quad \widetilde{\boldsymbol{e}} = \sum_i \boldsymbol{e}^i \tag{38}$$

where $\widetilde{\boldsymbol{e}}$ is the regular part of $\boldsymbol{e}$, which is the sum of all regular phase gradients $\boldsymbol{e}^i$. Contrarily to the case of perfect interface, the sum $\sum_i (\boldsymbol{n}\delta)_{\Gamma_i}\theta^i$ is no more null, due to the step of temperature at the Kapitza type boundary.

Next, we shall establish an integral equation for $\widetilde{\boldsymbol{e}}$ instead of $\boldsymbol{e}$. Substituting (38) into (29) yields

$$\widetilde{\boldsymbol{e}} = \boldsymbol{E} + 2\sum_i (\boldsymbol{n}\delta)_{\Gamma_i}\theta^i - 2\boldsymbol{P} * \sum_i (\boldsymbol{n}\delta)_{\Gamma_i}\theta^i + 2\boldsymbol{R} * \sum_i (\boldsymbol{n}\delta)_{\Gamma_i}\boldsymbol{e}^i \tag{39}$$

Now assuming that the Kapitza relation holds at the interface (see Fig. 2), the temperature jump at the interface is proportional to the normal flux by the relation

$$k^s_{ij}(\theta^j - \theta^i) = k_i \boldsymbol{e}^i \boldsymbol{n}_{\Gamma_{ij}} = k_j \boldsymbol{e}^j \boldsymbol{n}_{\Gamma_{ij}} \quad \text{on } \Gamma_{ij} \tag{40}$$

where k^s_{ij} is the interface Kapitza constant. Using the projector $\boldsymbol{n} \otimes \boldsymbol{n}$, we obtain

$$k^s_{ij}(\theta^j - \theta^i)\boldsymbol{n}_{\Gamma_{ij}} = k_i(\boldsymbol{n} \otimes \boldsymbol{n})_{\Gamma_{ij}}\boldsymbol{e}^i = k_j(\boldsymbol{n} \otimes \boldsymbol{n})_{\Gamma_{ij}}\boldsymbol{e}^j \quad \text{on } \Gamma_{ij} \tag{41}$$

Due to the fact that $\widetilde{\boldsymbol{e}} = \sum_i \boldsymbol{e}^i$ equal to $\boldsymbol{e}^i$ and $\boldsymbol{e}^j$ on each side of Γ_{ij}, the relation

$$(\boldsymbol{n} \otimes \boldsymbol{n}\delta)_{\Gamma_{ij}}\widetilde{\boldsymbol{e}} = (\boldsymbol{n} \otimes \boldsymbol{n}\delta)_{\Gamma_{ij}}(\boldsymbol{e}^i + \boldsymbol{e}^j) \tag{42}$$

must be verified. As a result the interface term $\sum(\boldsymbol{n}\delta)_{\Gamma_i}\theta^i$ does not vanish

but can be written as

$$\sum_i (\boldsymbol{n}\delta)_{\Gamma_i}\theta^i = \sum_{(i,j)} (\boldsymbol{n}\delta)_{\Gamma_{ij}}(\theta^i - \theta^j) = -\sum_{(i,j)} \frac{1}{\frac{k^s_{ij}}{k_i} + \frac{k^s_{ij}}{k_j}} (\boldsymbol{n}\otimes\boldsymbol{n}\delta)_{\Gamma_{ij}}\widetilde{\boldsymbol{e}} \tag{43}$$

Finally, combining with the previous expression (39), we can derive the equation for $\widetilde{\boldsymbol{e}}$ as follows

$$\begin{aligned}\widetilde{\boldsymbol{e}} = \boldsymbol{E} - 2\sum_{(i,j)} \frac{1}{\frac{k^s_{ij}}{k_i} + \frac{k^s_{ij}}{k_j}} (\boldsymbol{n}\otimes\boldsymbol{n}\delta)_{\Gamma_{ij}}\widetilde{\boldsymbol{e}} + 2\boldsymbol{P} * \sum_{(i,j)} \frac{1}{\frac{k^s_{ij}}{k_i} + \frac{k^s_{ij}}{k_j}} (\boldsymbol{n}\otimes\boldsymbol{n}\delta)_{\Gamma_{ij}}\widetilde{\boldsymbol{e}} \\ -2\boldsymbol{R} * \sum_{(i,j)} \frac{k_i - k_j}{k_i + k_j} (\boldsymbol{n}\delta)_{\Gamma_{ij}}\widetilde{\boldsymbol{e}}\end{aligned} \tag{44}$$

As a particular case, we can show that when $k^s_{ij} \to \infty$ and none of the joining materials has an infinite conductivity, the term $\frac{1}{\frac{k^s_{ij}}{k_i} + \frac{k^s_{ij}}{k_j}} \to 0$, and we recover the case of ideal interface.

In more explicit form, Eq. (44) reads

$$\begin{aligned}\widetilde{\boldsymbol{e}}(\boldsymbol{x}) = \boldsymbol{E} - 2\sum_{(i,j)} \frac{k_i - k_j}{k_i + k_j} \int_{\Gamma_{ij}} \boldsymbol{R}(\boldsymbol{x}-\boldsymbol{y})[\widetilde{\boldsymbol{e}}(\boldsymbol{y})\boldsymbol{n}(\boldsymbol{y})]d\boldsymbol{y} - \\ -2\sum_{(i,j)} \frac{1}{\frac{k^s_{ij}}{k_i} + \frac{k^s_{ij}}{k_j}} \int_{\Gamma_{ij}} \boldsymbol{P}(\boldsymbol{x}-\boldsymbol{y})[\boldsymbol{n}(\boldsymbol{y})\otimes\boldsymbol{n}(\boldsymbol{y})\widetilde{\boldsymbol{e}}(\boldsymbol{y})]d\boldsymbol{y}\end{aligned} \tag{45}$$

3.4. Iteration schemes

As an iteration method for perfect interface case (36), we can adopt the Neumann series based, or shortly basic iteration scheme.

Algorithm 1 Iteration scheme of problem with perfect interface

Initialization $\boldsymbol{e}^{(0)} = \boldsymbol{E}$
for m=0,1,2,... **do**
  $\boldsymbol{e}^{(m+1)} = \boldsymbol{E} - 2\boldsymbol{R} * \sum_{i,j} \frac{k_i - k_j}{k_i + k_j} (\boldsymbol{n}\delta)_{\Gamma_{ij}} \boldsymbol{e}^{(m)}$,
  if $\frac{\|\boldsymbol{e}^{(m+1)} - \boldsymbol{e}^{(m)}\|}{\|\boldsymbol{e}^{(m+1)}\|} < \varepsilon$ **then**
    BREAK
  end if
end for

Let us examine the property of the iteration scheme. First, due to the property of operators $\boldsymbol{P}$ and $\boldsymbol{R}$, $\widehat{\boldsymbol{e}}^{(m+1)}(\boldsymbol{\xi})$ is colinear with $\boldsymbol{\xi}$ and thus $\boldsymbol{e}^{(m+1)}$ is integrable

$$i\boldsymbol{\xi} \times \widehat{\boldsymbol{e}}^{(m+1)}(\boldsymbol{\xi}) = 0 \quad \text{or} \quad \text{rot } \boldsymbol{e}^{(m+1)} = 0 \tag{46}$$

Now taking the divergence of both side

$$\text{div } \boldsymbol{e}^{(m+1)} = -2 \sum_{i,j} \frac{k_i - k_j}{k_i + k_j} (\boldsymbol{n}\delta)_{\Gamma_{ij}} \boldsymbol{e}^{(m)} \tag{47}$$

Because $(\boldsymbol{n}\delta)_{\Gamma_{ij}} \boldsymbol{e}^{(m)}$ are terms localized on the interface Γ_{ij}, they and their gradients vanish outside this interface. As a result

$$\text{div } \boldsymbol{e}^{(m+1)} = 0 \quad \text{outside } \Gamma_{ij} \tag{48}$$

meaning that the flux $\boldsymbol{j}^{(n+1)} = k\boldsymbol{e}^{(n+1)}$

$$\text{div } \boldsymbol{j}^{(m+1)} = 0 \quad \text{in each phase } i \tag{49}$$

where the conductivity is a constant k_i.

Finally, these results show that the conservation of energy and compatibility of the gradient of temperature are verified at each iteration inside each

phase domain. The iterative process allows us to check that the conditions of energy and compatibility are also verified at the interfaces when the convergence is reached.

Regarding the stopping criteria, we have

$$\text{Error} = \frac{\|\boldsymbol{e}^{(m+1)} - \boldsymbol{e}^{(m)}\|}{\|\boldsymbol{e}^{(m+1)}\|} < \varepsilon \tag{50}$$

We note that $\boldsymbol{r}^{(m)} = \boldsymbol{e}^{(m+1)} - \boldsymbol{e}^{(m)}$ is the residual at step m. Near convergence, the behavior of Error is expected to be the same as the one of the residual $\boldsymbol{r}^{(m)}$.

To solve the problem involving interface (44), numerical evidences show that the above iteration scheme does not converge. To solve the equations, we use conjugated gradient methods. The governing equation (44) can be recast into the linear form

$$\boldsymbol{A} \odot \widetilde{\boldsymbol{e}} = \boldsymbol{E} \tag{51}$$

with

$$\begin{aligned}\boldsymbol{A} \odot \widetilde{\boldsymbol{e}} = \widetilde{\boldsymbol{e}} + 2\sum_{(i,j)} \frac{1}{\frac{k^s_{ij}}{k_i} + \frac{k^s_{ij}}{k_j}} (\boldsymbol{n} \otimes \boldsymbol{n}\delta)_{\Gamma_{ij}} \widetilde{\boldsymbol{e}} - 2\boldsymbol{P} * \sum_{(i,j)} \frac{1}{\frac{k^s_{ij}}{k_i} + \frac{k^s_{ij}}{k_j}} (\boldsymbol{n} \otimes \boldsymbol{n}\delta)_{\Gamma_{ij}} \widetilde{\boldsymbol{e}} \\ +2\boldsymbol{R} * \sum_{(i,j)} \frac{k_i - k_j}{k_i + k_j} (\boldsymbol{n}\delta)_{\Gamma_{ij}} \widetilde{\boldsymbol{e}}\end{aligned} \tag{52}$$

The linear equation (51) will be solved by the conjugate gradient stabilized algorithm.

Algorithm 2 Biconjugate gradient stabilized (BICGSTAB) iteration scheme for imperfect interface problem with linear equation $\boldsymbol{A} \odot \widetilde{\boldsymbol{e}} = \boldsymbol{E}$

Initialization $\widetilde{\boldsymbol{e}}^{(0)} = \boldsymbol{0}$
$\boldsymbol{r}^{(0)} = \boldsymbol{E}$ and choose $\boldsymbol{r}' = \boldsymbol{r}^{(0)}$
Set $\boldsymbol{p}^{(0)} = \boldsymbol{r}^{(0)}$
for m=0,1,2,... **do**
1. $\alpha^{(m)} = (\boldsymbol{r}^{(m)}\boldsymbol{r}')/((\boldsymbol{A} \odot \boldsymbol{p}^{(m)})\boldsymbol{r}')$,
2. $\boldsymbol{s}^{(m)} = \boldsymbol{r}^{(m)} - \alpha^{(m)}(\boldsymbol{A} \odot \boldsymbol{p}^{(m)})$
if $\|\boldsymbol{s}^{(m)}\|/\|\boldsymbol{E}\| < \varepsilon$ **then**
$\widetilde{\boldsymbol{e}}^{(m+1)} = \widetilde{\boldsymbol{e}}^{(m)} + \alpha^{(m)}\boldsymbol{p}^{(m)}$
BREAK
end if
3. $\gamma^{(m)} = ((\boldsymbol{A} \odot \boldsymbol{s}^{(m)})\boldsymbol{s}^{(m)})/((\boldsymbol{A} \odot \boldsymbol{s}^{(m)})(\boldsymbol{A} \odot \boldsymbol{s}^{(m)}))$
4. $\widetilde{\boldsymbol{e}}^{(m+1)} = \widetilde{\boldsymbol{e}}^{(m)} + \alpha^{(m)}\boldsymbol{p}^{(m)} + \gamma^{(m)}\boldsymbol{s}^{(m)}$
5. $\boldsymbol{r}^{(m+1)} = \boldsymbol{s}^{(m)} - \gamma^{(m)}(\boldsymbol{A} \odot \boldsymbol{s}^{(m)})$
if $\|\boldsymbol{r}^{(m+1)}\|/\|\boldsymbol{E}\| < \varepsilon$ **then**
BREAK
end if
6. $\beta^{(m)} = \alpha^{(m)}/\gamma^{(m)}(\boldsymbol{r}^{(m+1)}\boldsymbol{r}')/(\boldsymbol{r}^{(m)}\boldsymbol{r}')$
7. $\boldsymbol{p}^{(m+1)} = \boldsymbol{r}^{(m+1)} + \beta^{(m)}(\boldsymbol{p}^{(m)} - \gamma^{(m)}\boldsymbol{A} \odot \boldsymbol{p}^{(m)})$
if $\|\boldsymbol{r}^{(m+1)}\boldsymbol{r}'\|/\|\boldsymbol{E}\|^2 < \varepsilon'$ **then**
$\boldsymbol{r}' = \boldsymbol{r}^{(m+1)}$
$\boldsymbol{p}^{(m+1)} = \boldsymbol{r}^{(m+1)}$
end if
end for

Introducing a tolerance ε, the scheme is based on the residual $\boldsymbol{r}^{(j+1)}$ and stopped when

$$\text{Error} = \frac{\|\boldsymbol{r}^{(m+1)}\|}{\|\boldsymbol{E}\|} < \varepsilon \tag{53}$$

In most usual cases, the parameter ε' to restart in case of breakdown is set at $\varepsilon' = 10^{-6}$. In the cases of Kapitza interfaces, to ensure the convergence at low value k_s, we adopt a higher value $\varepsilon' = 10^{-3}$.

The use of BICGSTAB algorithm merits some discussion at this step. In literature, Zeman et al. (2010) applied the standard conjugate gradient (CG) scheme to the basic integral equation of (Michel et al., 2000) which has a non symmetric operator. They found that the scheme converges with a moderate contrast ratio but diverges at infinite contrast limit. Schneider (2020) reconsidered the case of porous material with different discretization techniques and iterative schemes and found that the Fourier discretization results in bad convergence behavior. Adopting finite difference or finite element discretization results in a better behavior. Lucarini et al. (2022) also confirm this remark and additionally proposed a displacement based scheme for the solid phase which works for Fourier discretization. Their displacement scheme is derived directly from the Navier equation without using the Green tensors. The present formulation is based on the Green tensors and the problem aims at solving the composite problems at two extreme limits where pore, superconductive phase and imperfect interface can be all present. The operator is non symmetric and the Fourier discretization is used. As it will be shown, the simple iterative scheme is sufficient to overcome the issues of previous schemes in the case of perfect interfaces. In addition, the BICGSTAB algorithm is expected to overcome the difficulties in the above discussion even in the case of imperfect interfaces.

All the calculations are done in Fourier space, as we compute $\widehat{\widetilde{\boldsymbol{e}}}(\boldsymbol{\xi})$ and $\widehat{\boldsymbol{e}}(\boldsymbol{\xi})$ at base resolution N. This parameter is used to limit the number of wave vectors in directions $1, 2, 3$ in (3) via the inequality

$$-N < n_k \leq N \quad k = 1, 2, 3. \tag{54}$$

To achieve the accuracy, the delta terms $\widehat{(\boldsymbol{n} \otimes \boldsymbol{n}\delta)}_{\Gamma_{ij}}(\boldsymbol{\xi})$ and $\widehat{(\boldsymbol{n}\delta)_{\Gamma_{ij}}}(\boldsymbol{\xi})$ have a double resolution $2N$. The Fourier transform of the real space product between those delta terms and the gradient $\boldsymbol{e}$ (or $\widetilde{\boldsymbol{e}}$) is done via (5) and (6). After the resolution of $\boldsymbol{e}$ in Fourier space, the temperature field θ is recovered

via the relation

$$\theta = -\boldsymbol{R} * \boldsymbol{e}, \quad \text{or} \quad \widehat{\theta}(\boldsymbol{\xi}) = -\widehat{\boldsymbol{R}}(\boldsymbol{\xi})\widehat{\boldsymbol{e}}(\boldsymbol{\xi}) \tag{55}$$

in Fourier space. Finally, the physical fields can be obtained by inverse Fourier transform. Numerically, we employ Discrete Fourier Transform (DFT) and obtain the discrete values of the field at grid points $\bar{\boldsymbol{x}}$. For function $\widehat{\varphi}(\boldsymbol{\xi})$, we have

$$\varphi(\bar{\boldsymbol{x}}) \simeq \mathrm{DFT}^{-1}[\widehat{\varphi}(\boldsymbol{\xi})] \tag{56}$$

It is known that the use of Fourier series is associated to ring artifacts when discontinuities are present. To smooth out the function $\varphi(\boldsymbol{x})$, we will use a sinc filter $\widehat{f}(\boldsymbol{\xi})$ in frequency domain (To and Bonnet, 2023b) as follows

$$\varphi(\bar{\boldsymbol{x}}) \simeq \mathrm{DFT}^{-1}[\widehat{f}(\boldsymbol{\xi})\widehat{\varphi}(\boldsymbol{\xi})] \tag{57}$$

with $\widehat{f}(\boldsymbol{\xi})$ being

$$\widehat{f}(\boldsymbol{\xi}) = \mathrm{sinc}(\xi_1 a)\mathrm{sinc}(\xi_2 a)\mathrm{sinc}(\xi_3 a) \tag{58}$$

The typical value of a is $a = L/2N$ which is the size of the pixel.

4. Numerical applications

The following results are valid for any unit systems. For the ease of reading, the SI system is adopted as follows:
- Length, distance, coordinate: [m]
- Fourier classical conductivity: [W/m·K]
- Kapitza interface conductivity: [W/m^2·K]
- Temperature: [K]
- Temperature gradient: [K/m]

4.1. Perfect interface

We consider the 2D case of single circular inclusion embedded in a matrix of different material. The unit cell is defined by the inequalities $|x| \leq L_1/2$ and $|y| \leq L_2/2$. The center of the inclusion is located at the origin of the unit cell. The radius of the inclusion is $R = 0.3$ [m] and the unit cell dimension $L_1 = L_2 = L = 1$ [m]. The conductivity of the matrix is set at $k_m = 1$ [W/m·K] and the inclusion k_i is varied from 0 to ∞. We study the accuracy of the FFT method in comparison with a Finite Element Method code (COMSOL). Since the FEM code does not allow us using these extreme values 0 and ∞ (infinite contrast), we shall use the value $k_i = 10^{-6}$ [W/m·K] and $k_i = 10^6$ [W/m·K] (very high contrast) correspondingly (see Appendix C for the FEM model). Separate simulations where the inclusion domain is removed and Neumann or Dirichlet boundary conditions are used to reproduce the effect of infinite contrast have shown that the obtained solutions in the matrix phase are almost identical to the case of very high contrast. Since we are interested in the FEM and FFT solutions in the inclusion domain to examine the solution uniqueness in the extreme cases, the solution at high contrast ratio instead of infinite contrast ratio will be presented. As discussed earlier, unlike the usual setting of the problem where $\boldsymbol{e}$ is not unique in the pore, the solution $\boldsymbol{e}$ of the present FFT formulation must be a harmonic continuation into the pore and thus is unique if the pore is a simply connected domain. The macroscopic gradient $E_1 = 1, E_2 = 0$ [K/m] is applied to the unit cell. The basic iteration scheme (Algorithm 1) is used to obtain the solution.

The simple iterative algorithm is very fast; it only needs 10 iterations to satisfy the accuracy $\varepsilon = 10^{-5}$ for both cases $k_i = 0$ [W/m·K] and $k_i = \infty$ [W/m·K]. These results show a clear improvement compared to previous formulations using FFT method where the classical iterative scheme does not converge in numerous cases.

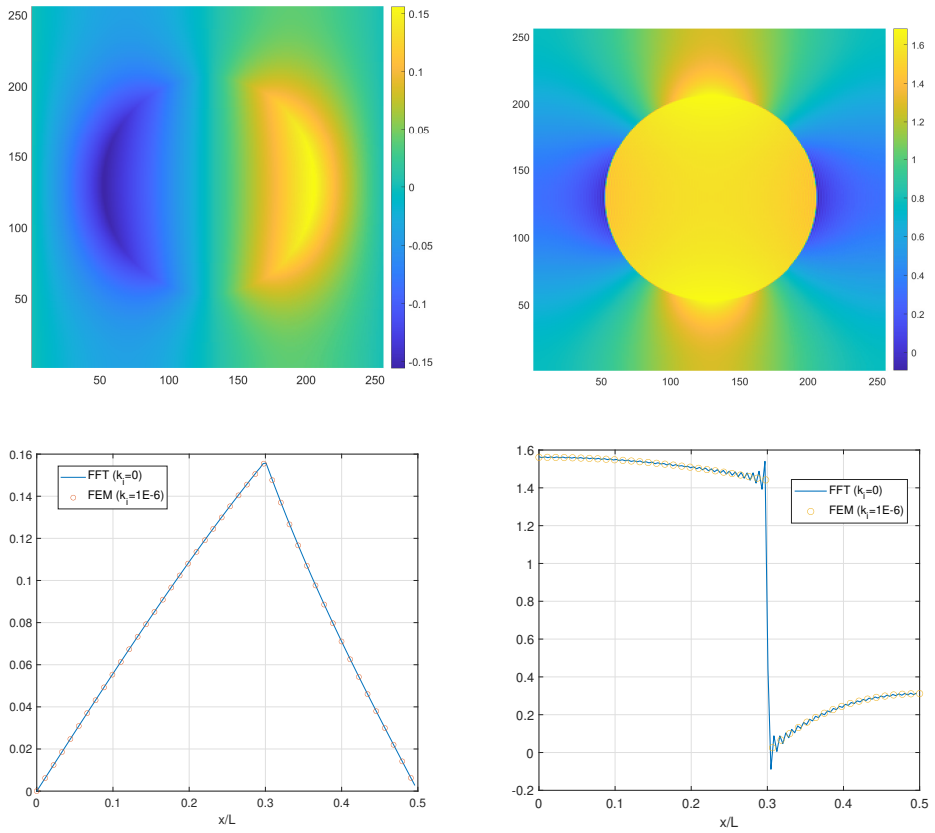

Figure 3: The case of circular void $k_i = 0$ [W/m·K]. Top: Temperature field θ [K] (left) and gradient field e_1 [K/m] (right). Bottom: Comparison between FFT and FEM solutions for temperature θ [K] (left) and gradient e_1 [K/m] (right) profile at $y = 0$. The FFT solution is obtained at resolution $N = 128$.

In Figs. 3 and 4, we can find that the periodic perturbation temperature field θ is continuous and increasing in the same direction as E_1 when $k_i = 0$ [W/m·K] and in the opposite direction when $k_i = \infty$ [W/m·K]. The gradient $e_1 = 0$ [K/m] in the inclusion when $k_i = \infty$ [W/m·K] corresponds to linear temperature θ and agrees with the FEM results. When $k_i = 0$ [W/m·K], the agreement between FEM and FFT is also excellent. This confirms that the solution of the LS formulation exists uniquely and is the limit of the solution at finite k_i and $k_i \to 0$ [W/m·K]. In all figures, the FFT solution is smooth for the temperature field which is theoretically continuous and the gradient $\boldsymbol{e}$ exhibits some local fluctuations near the interface due to the Gibbs phenomenon and the discontinuity. We note that the fluctuation can be smoothed out using a low pass filter, as shown thereafter.

From Fig. 5, we find that the basic iteration scheme for perfect interface converges very fast. The error decreases at a linear rate up to 30-40 iterations to reach the accuracy 10^{-15}. The ratios related to inverse contrasts, i.e $k_i/k_m = 10$ vs $k_i/k_m = 0.1$ (or $k_m/k_i = 10$) and $k_i/k_m = 0$ vs $k_i/k_m = \infty$ (or $k_m/k_i = 0$) have the same convergence rate. The two infinite contrast cases converge slower than the finite contrast cases, Error $\propto 10^{-N_{iter}/2.5}$ and $\propto 10^{-N_{iter}/2}$ respectively. Next we study the resolution effect at infinite contrast case $k_i/k_m = \infty$ and we find that a fine resolution N leads to a faster convergence than a coarse resolution. In all cases, the relative error is stabilized at 10^{-15} after 40 iterations.

The nearly linear decrease of the error in the semi-log plot can be explained by the fact that the convergence is driven by the highest eigenvalue of the iterative operator. With these results, this highest eigenvalue is obtained as $\lambda_{max} \approx 0.40$ for the infinite contrast and $\lambda_{max} \approx 0.32$ for the finite contrast. The comparison with the basic iteration scheme for the classical FFT solution where the highest eigenvalue tends to 1 for an infinite contrast (Michel et al.,

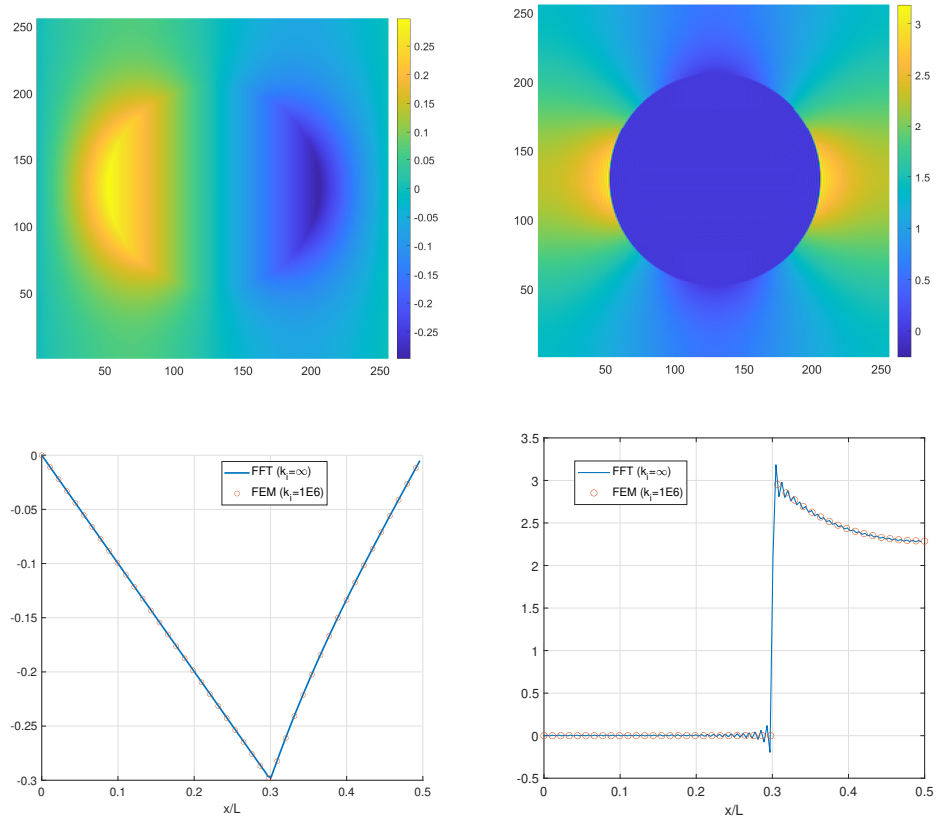

Figure 4: The case of circular superconductive inclusion $k_i = \infty$ [W/m·K]. Top: Temperature field θ [K] (left) and gradient field e_1 [K/m](right). Bottom: Comparison between FFT and FEM for temperature θ [K] (left) and gradient e_1 [K/m] (right) profile at $y = 0$. The FFT solution is obtained at resolution $N = 128$.

2001) displays clearly the improvement coming from the present boundary-volume formulation.

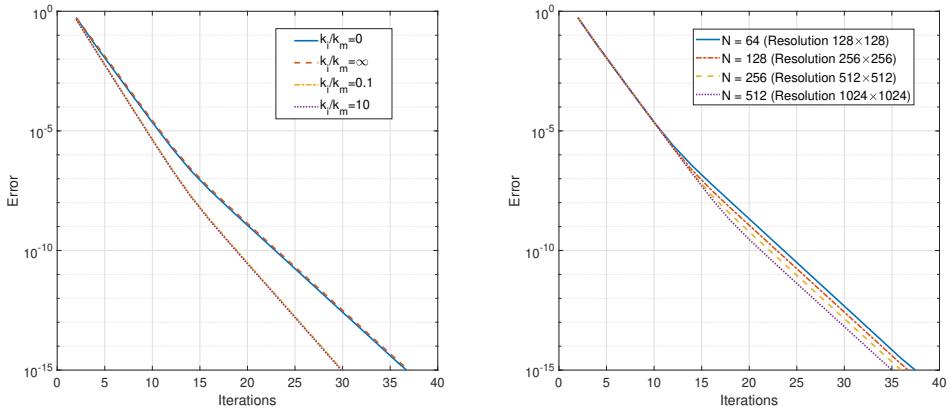

Figure 5: Convergence of basic iteration scheme for circular inclusion with perfect interface problem. Left: Cases of different constrast ratios k_i/k_m at $N = 128$. Right: Cases of different resolution parameters N at ratio $k_i/k_m = \infty$

Next, we investigate the effect of smoothing filter and the mesh convergence of the two extreme problems. The gradient field e_1 will be considered when discontinuities are present at the interface. First from Fig. 6, we notice that at all resolutions, the FFT solutions are quite good far from the interface as they all match the FEM results. The main visible difference is seen near the interface. The sinc filter does eliminate the ring artifact but it also reduces the jump at the interface and produces a gradual 'interphase like' change. As expected, when the resolution increases, the interphase becomes thinner and converges to a sharp interface with correct jump value. For both extreme cases, the resolution $N = 128$ produces sufficiently accurate results.

4.2. Kapitza interface model

In this subsection, we shall study two examples in the unit cell of dimensions $L_1 = L_2 = L = 1$ [m] as before. In the first example, a stratified

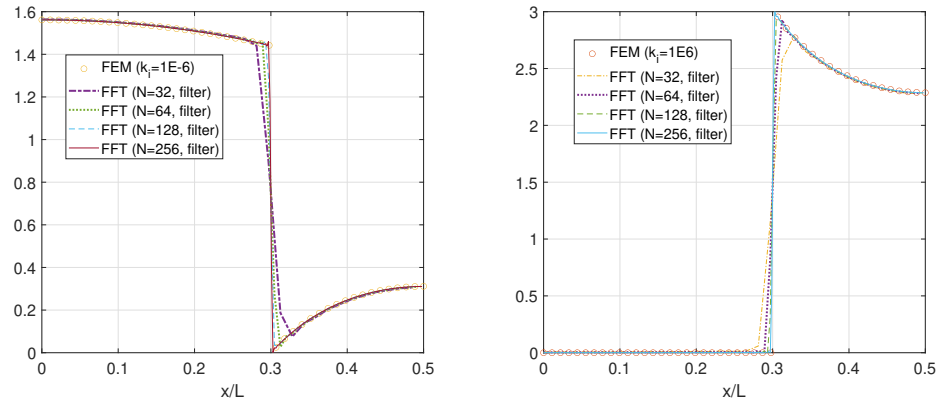

Figure 6: Mesh convergence and smoothing filter effect for circular inclusion with perfect interface problem. Left: the gradient e_1 [K/m] as function of x/L at $y = 0$ [m] for the case of void inclusion $k_i = 0$ [W/m·K]. Right: the gradient e_1 [K/m] as function of x/L at $y = 0$ [m] for the case of superconductive inclusion $k_i = \infty$ [W/m·K]

material is composed of inclusion and matrix layers. The inclusion is located at the center and has a thickness $2h = 0.6$ [m], i.e $|y| \leq h = 0.3$ [m]. In the second example, an inclusion circle of radius $R = 0.3$ [m] is located at the center and bounded by the matrix, i.e the same geometries as subsection 1. In both cases, the conductivity of each material is inclusion $k_i = 10$ [W/m·K], matrix $k_m = 1$ [W/m·K] and the imperfect interface between the matrix and inclusion is modelled by Kapitza model with $k_s = 1$ [W/m^{2}K]. The macroscopic gradient $E_1 = 1$ [K/m], $E_2 = 0$ [K/m] is applied to the unit cell. While the first example has analytical solutions (see Appendix B) and can be used to compare with the FFT solution, only numerical FEM solution is available in the other case. The BICGSTAB algorithm (Algorithm 2) is used to obtain the solution.

For the stratified problem (see Fig. 7), we only need 4 iterations to reach the accuracy $\varepsilon = 10^{-5}$. As we can see from the temperature field which is piece-wise linear, discontinuities are present near the interface and temperature on the left is higher than on the right. The gradient field is regular,

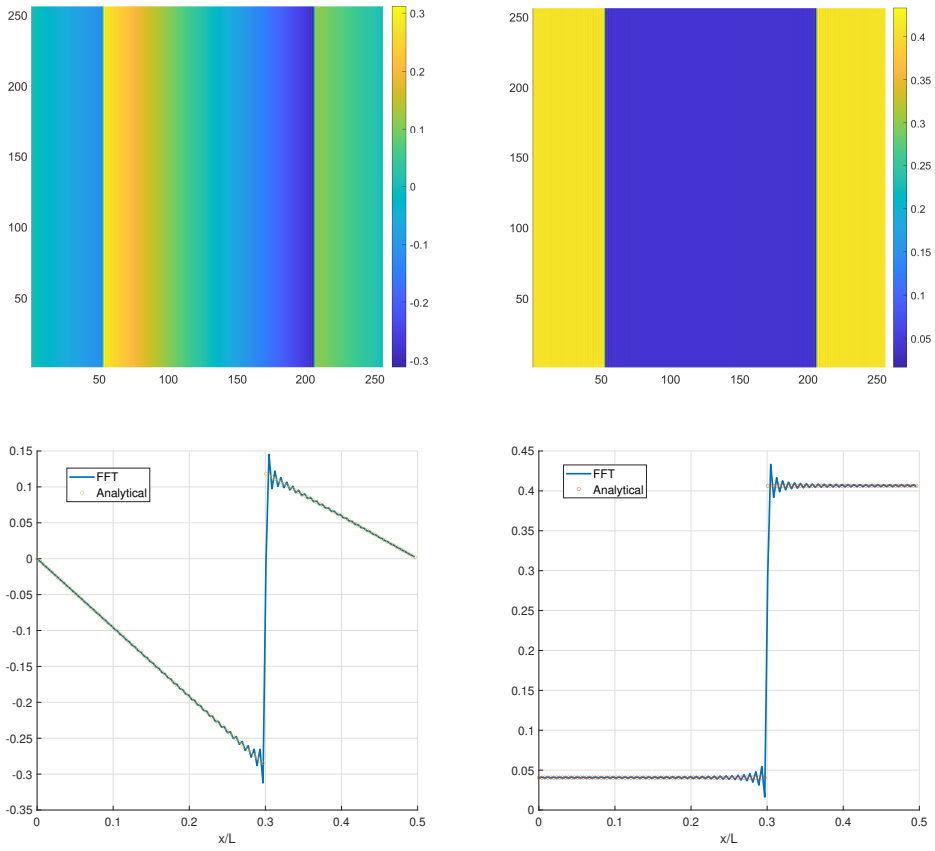

Figure 7: Stratified material problem with Kapitza interface model. Top: Temperature field θ (left) and regular gradient field $\widetilde{e}_1$ (right). Bottom: Comparison between analytical solution and FFT solutions for temperature θ [K] (left) and regular gradient $\widetilde{e}_1$ [K/m] (right) profile at $y = 0$

exhibiting no singularities at the interface and being uniform in each layer. The slice in the middle also confirms those properties and agrees very well with the analytical results (see Appendix B).

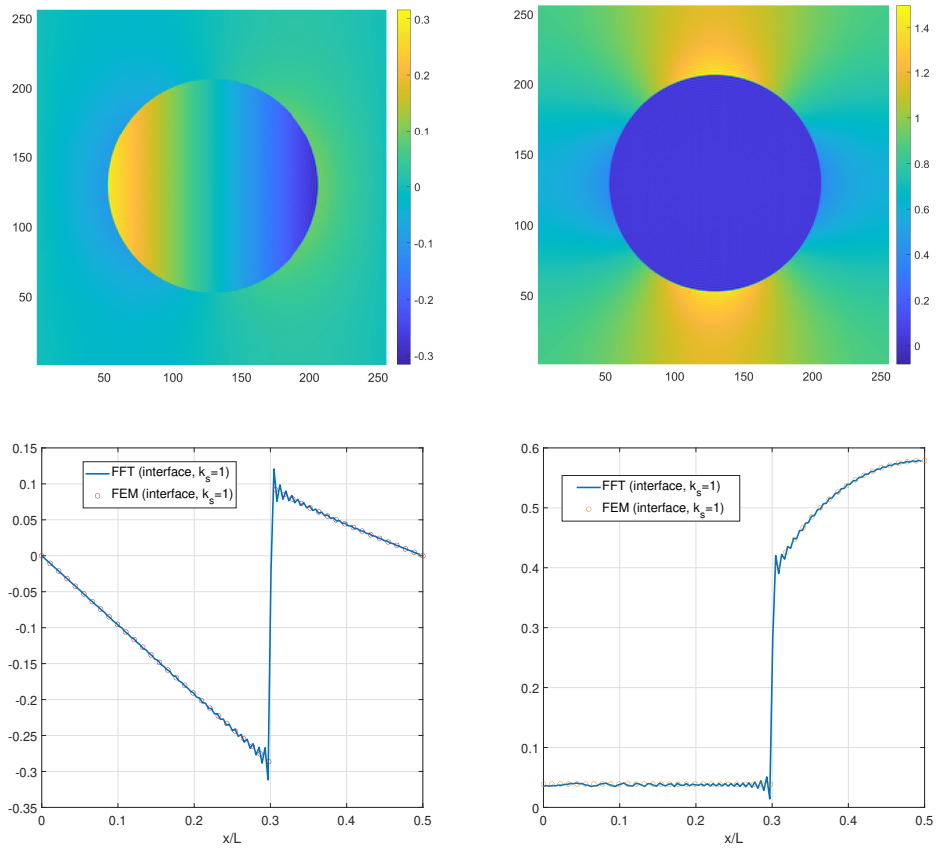

Figure 8: Circular inclusion problem with Kapitza interface model. Top: Temperature field θ (left) and regular gradient field $\widetilde{e}_1$ (right). Bottom: Comparison between FEM and FFT for temperature θ [K] (left) and regular gradient $\widetilde{e}_1$ [K/m] (right) profile at $y = 0$. The interface coefficient $k_s = 1$ [W/m^{2}K]

In the circular inclusion problem (see Fig. 8), only 13 iterations are needed to reach the accuracy level $\varepsilon = 10^{-5}$. The same remarks apply to this problem: interface discontinuities are found on the temperature field θ while the

gradient field $\widetilde{e}_1$ does not display any singularity. The gradient level in the inclusion is relatively smaller than within the matrix. More importantly, the temperature and the gradient profiles on the axis $y = 0$ are in a very good agreement with the FEM models containing an interphase.

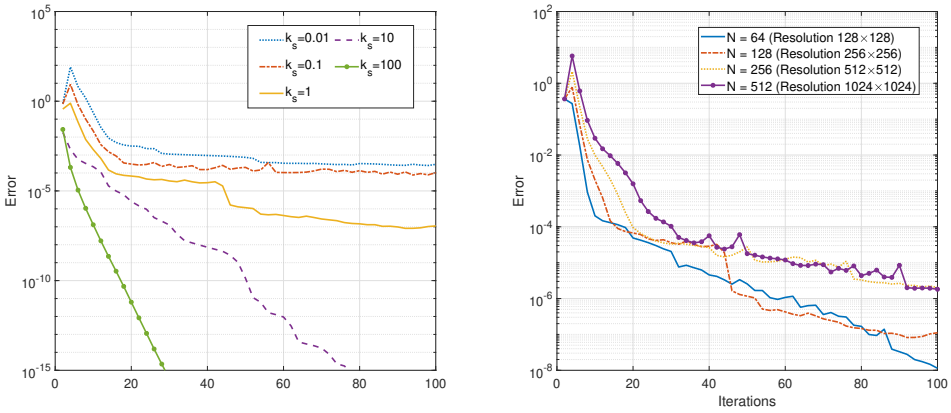

Figure 9: Convergence of BICGSTAB scheme for circular inclusion with Kapitza interface problem. Left: Cases of different interface coefficient k_s at $N = 128$. Right: Cases of different resolution parameters N at $k_s = 1$ [W/m^{2}K]. The unit of k_s is [W/m^{2}K] in all the figures.

From Fig. 9, we find that the convergence rate of BICGSTAB scheme is also very good but is sensitive to the interface coefficient k_s. With large k_s, i.e when the interface is closer to the ideal interface, the convergence is very fast, for example the residual error scales as Error $\propto 10^{-N_{iter}/2}$ for $k_s = 100$ [W/m^{2}K], $10^{-N_{iter}/6}$ for $k_s = 10$ [W/m^{2}K] etc. With small k_s, the interface is approaching a closed circular crack where the problem has no unique solution on the boundary and within the inclusion phase. As a consequence, the convergence becomes significantly delayed. For example to reach 10^{-3} error level, 10,15 and 40 iterations are required for $k_s = 1$, 0.1 and 0.01 [W/m^{2}K] respectively. Regarding the resolution number N, the convergence is slightly sensitive to this parameter. The difference between the results coming from different resolution numbers is seen in the initial steps where the low reso-

lution shows a steeper descent. However, after 40 iterations, they tend to decrease with the same rate, especially for the two high resolutions 512×512 and 1024×1024 that nearly coincide after 40 iterations.

4.3. Multiple phase composites with infinite contrast ratios and imperfect interface

We are interested in the performance of the method when there are multiple phases present in the unit cell, comprising simultaneously voids and superconducting inclusions. In the first example, we consider a matrix inclusion structure, specifically a composite constituted of an array of 9 circular inclusions of dimension $R = 0.1$ [m] of different properties: 1 circular void ($k = 0$ [W/m·K]) at the center, 4 superconductive inclusions ($k = \infty$ [W/m·K]) and 4 conductive inclusions ($k = 5$ [W/m·K]) embedded in the matrix material ($k = 1$ [W/m·K]). The material is subject to macroscopic gradient $E_1 = E_2 = 1$ [K/m]. As expected (see Fig. 10), the gradients in the inclusions are more or less uniform with small value in superconductive phase and higher value in the void. Although the basic scheme is relatively good, it is outperformed by the BICGSTAB algorithm. After a steep descent at 10^{-4}, the basic scheme changes its slope and converges much slower, reaching 10^{-6} only after 1000 iterations. The BICGSTAB algorithm keeps the steep descent and the error level 10^{-15} can be reached after 330 iterations. These results show that the convergence is degraded with the simultaneous presence of voids and superconductive inclusions, compared to the case of an unique type of inclusion.

Next, we consider a checker board structure constituted of 9 squares of dimensions $1/3 \times 1/3$ [m]. The square at the center is a void $k = 0$ [W/m·K] and the 8 surrounded squares have a conductivity $k = 1$ [W/m·K] or $k = 2$ [W/m·K]. Both the perfect and imperfect interface are used to model the interfaces between the phases of different conductivity, i.e $k = 1$ [W/m·K] and $k = 2$ [W/m·K]. From Figs. 11, we can clearly see the effect of interface.

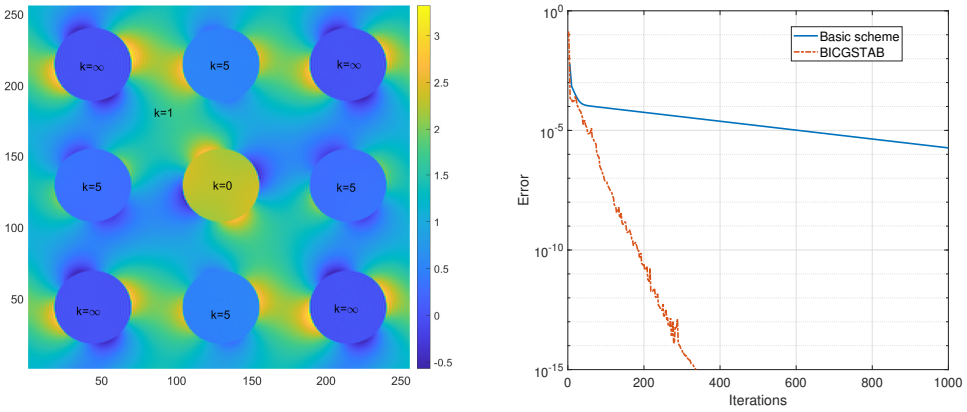

Figure 10: Composites subject to a macroscopic gradient $E_1 = E_2 = 1$ [K/m]. Left: Gradient field e_1 [K/m]. Right: Comparison between basic and BICGSTAB scheme.

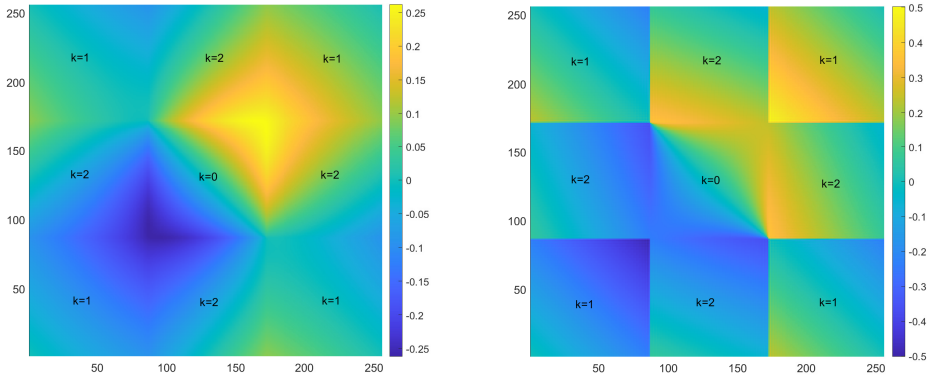

Figure 11: Temperature field θ of composites subject to a macroscopic gradient $E_1 = E_2 = 1$ [K/m]. Left: Perfect interface. Right: Imperfect interface with $k_s = 2$ [W/m^{2}K] between the squares $k = 1$ [W/m·K] and $k = 2$ [W/m·K].

For perfect interfaces, the temperature field varies continuously between the phases. For imperfect interface, a sharp contrast can be observed at the interface.

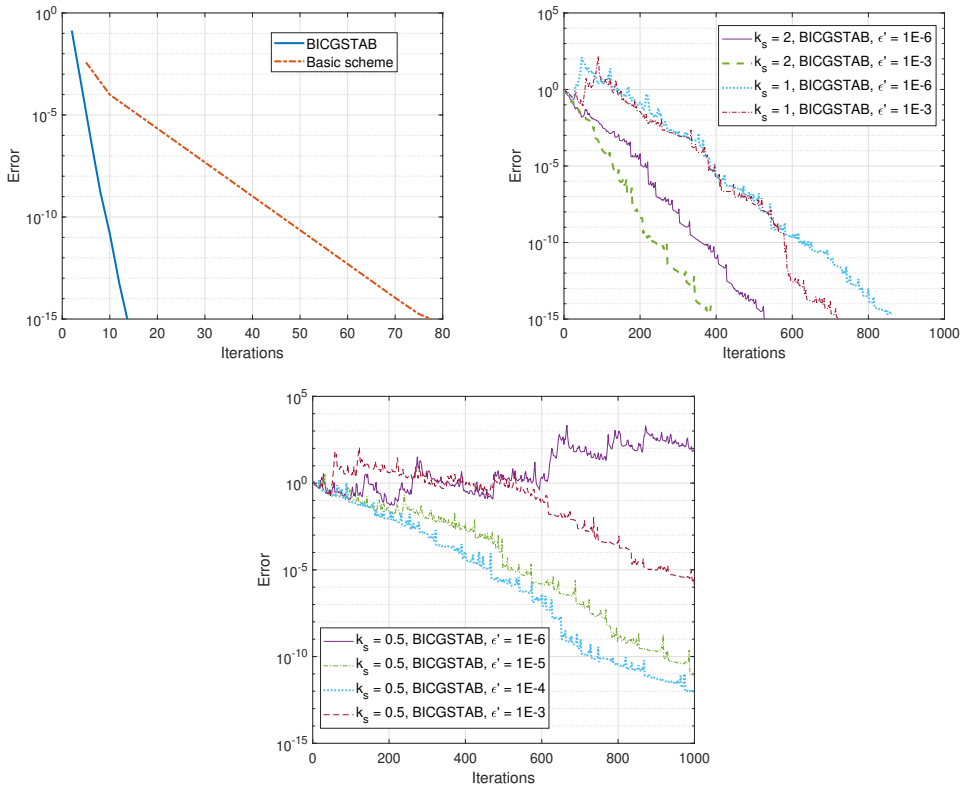

Figure 12: Composites with imperfect interface subject to a macroscopic gradient $E_1 = E_2 = 1$ [K/m]. Top left: Comparison between basic and BICGSTAB scheme. Top right: Comparison BICGSTAB scheme with $k_s = 1, 2$ [W/m^{2}K] and different value ε'. Bottom: Comparison BICGSTAB scheme with $k_s = 0.5$ [W/m^{2}K] and different value ε'. The unit of k_s is W/m^{2}K in all examples.

Figure 12 shows that for the case of perfect interface, the basic scheme converges very fast but the accuracy level is reached at 10^{-15} after 77 iterations. Again, the BICGSTAB algorithm converges much faster as 10^{-15} accuracy level is reached with less than 15 iterations. For the case of imperfect in-

terface, BICGSTAB is still robust as it reaches 10^{-15} accuracy level after 500-700 iterations. However, for low k_s value, the scheme is slower. This is due to the fact that the interfaces behave as cracks when $k_s \to 0$. The central squared phase become separated and the problem is ill posed in this extreme case. We tried to modify the restart parameters ε' and k_s and found that the convergence behavior can be sensitive to this change. For example, at $k_s = 1-2$ [W/m^{2}K], the choice $\varepsilon' = 10^{-3}$ results in a better convergence than $\varepsilon' = 10^{-6}$ in the first 1000 iterations. At $k_s = 0.5$ [W/m^{2}K], the convergence is even more sensitive to ε'. Within 1000 iterations, using $\varepsilon' = 10^{-6}$ does not yield convergence and $\varepsilon' = 10^{-3}$ performs better. The intermediate values $\varepsilon' = 10^{-4}, 10^{-5}$ give the best performance. This experience shows that it is possible to adjust ε' to achieve convergence.

5. Concluding remarks

In this paper, we have presented a boundary-volume FFT based method to solve homogenization problems related to heterogeneous conductive materials with arbitrary contrast and Kapitza interface model. Starting from the integral equation for a single homogeneous phase, a boundary-volume LS integral equation for the composite material is established. In the latter, the temperature gradient is the unknown and depends on the material mismatch quantities at the interface between two different phases. Both perfect interface and Kapitza imperfect interface models can be implemented using this formulation in a relatively simple way. More interestingly, the convergence of the iteration scheme is very fast even for the case of infinite contrast. In the case of materials containing only one type of inclusion (void or superconductive inclusion), the basic scheme of the FFT method leads fast to accurate results, this being a significant improvement compared to many formulations proposed in the literature that do not converge or converge only when using sophisticated numerical procedures. For the case of simultaneous voids and superconductive inclusions or the case of imperfect Kapitza interfaces, the

conjugate gradient method must be preferred.

Although the present work focuses on the linear behavior of conductive material, the derivation procedure suggests that the formulation can be generalized to include anisotropic effects and non-linear bulk and interface behaviors. Starting from equation for each phase Eq. (23), those effects can be treated as polarization in each phase as done in classical FFT approaches and then assembled to make up the final equation. In this case, a mixed boundary-domain formulation is obtained where the expression of $\boldsymbol{e}$ includes both surface and volume integrals. In addition, the phase conductivity can be viewed as reference conductivity which can be chosen different in different zones, allowing us to use Green tensors for both isotropic and anisotropic materials, these last ones being available. It will be interesting to know if the good convergence property is still maintained in such formulations.

The crucial points that lead to good convergence behavior are the governing equations (36), (44). The illustrative examples in this work concern the discretization in Fourier space of the equations and the use of form factors which are the Fourier transform of the geometry of the interfaces. Given any complex geometry including pixel/voxel based images, we can approximate with poly lines and poly surfaces and the same strategies can be applied (see e.g To and Bonnet, 2020, 2023b). The main drawback of the form factor approaches is the memory usage as a higher resolution must be adopted for the form factors. To overcome this difficulty, i.e to avoid evaluating the discrete convolution $(\boldsymbol{n}\delta)_{\Gamma_{ij}}$ and $\boldsymbol{e}$ in Fourier space, it is possible to construct a grid based approximation of the Fourier transform of $(\boldsymbol{n}\delta)_{\Gamma_{ij}}\boldsymbol{e}$ for both curve and pixel/voxel boundaries. Additionally, due to the similarity between the linear conduction and elasticity problem, the extension of this method to the case of mechanical behavior is also in progress.

Appendix A. Form factors of 2D geometries

Appendix A.1. Circles

Let us consider a circle Ω of radius R centered at origin of the square unit cell of dimension $L \times L$. The form factor of the circle is given by

$$\widehat{\chi}(\boldsymbol{\xi}) = \frac{1}{V}\int_{\Omega} e^{-i\boldsymbol{\xi}\boldsymbol{x}} d\boldsymbol{x} = \frac{2\pi R^2}{L^2}\frac{J_1(\xi R)}{\xi R}. \tag{A.1}$$

Using the Gauss theorem, the form factor of $(\boldsymbol{n}\delta)_\Gamma$ associated to the boundary Γ admits the form

$$\widehat{(\boldsymbol{n}\delta)_\Gamma}(\boldsymbol{\xi}) = \frac{1}{V}\int_{\Gamma} \boldsymbol{n} e^{-i\boldsymbol{\xi}\boldsymbol{x}} d\boldsymbol{x} = \frac{1}{V}\int_{\Omega} \nabla(e^{-i\boldsymbol{\xi}\boldsymbol{x}}) d\boldsymbol{x} = -i\boldsymbol{\xi}\chi(\boldsymbol{\xi}). \tag{A.2}$$

The form factor of $(\boldsymbol{n}\otimes\boldsymbol{n}\delta)_\Gamma$ can be evaluated as follows:

$$\begin{aligned}
&\widehat{(\boldsymbol{n}\otimes\boldsymbol{n}\delta)}_\Gamma(\boldsymbol{\xi}) = \frac{1}{V}\int_{\Gamma} \boldsymbol{n}\otimes\boldsymbol{n} e^{-i\boldsymbol{\xi}\boldsymbol{x}} d\boldsymbol{x} = \frac{1}{VR}\int_{\Gamma} \boldsymbol{n}\otimes\boldsymbol{x} e^{-i\boldsymbol{\xi}\boldsymbol{x}} d\boldsymbol{x} \\
&= \frac{1}{VR}\int_{\Omega} \nabla(\boldsymbol{x} e^{-i\boldsymbol{\xi}\boldsymbol{x}}) d\boldsymbol{x} = \frac{\chi(\boldsymbol{\xi})}{R}\boldsymbol{I} - \frac{i\boldsymbol{\xi}}{VR}\otimes\int_{\Omega} \boldsymbol{x} e^{-i\boldsymbol{\xi}\boldsymbol{x}} d\boldsymbol{x} \\
&= \frac{\chi(\boldsymbol{\xi})}{R}\boldsymbol{I} + \frac{\boldsymbol{\xi}}{R}\otimes\nabla_{\boldsymbol{\xi}}\chi(\boldsymbol{\xi}) = \frac{\chi(\boldsymbol{\xi})}{R}\boldsymbol{I} + \frac{\boldsymbol{\xi}\otimes\boldsymbol{\xi}}{\xi R}\frac{d\chi(\boldsymbol{\xi})}{d\xi}
\end{aligned} \tag{A.3}$$

with

$$\frac{d\chi(\boldsymbol{\xi})}{d\xi} = \frac{2\pi R^2}{L^2}\left[\frac{J_0(R\xi)}{\xi} - \frac{2J_1(R\xi)}{R\xi^2}\right]. \tag{A.4}$$

In the above derivation we use the fact that $\boldsymbol{n} = \boldsymbol{x}/R$ on the circle boundary and the Gauss theorem to convert surface to domain integral. Finally we obtain the form factor

$$\widehat{(\boldsymbol{n}\otimes\boldsymbol{n}\delta)}_\Gamma(\boldsymbol{\xi}) = \frac{2\pi R^2}{L^2}\left[\frac{J_1(R\xi)}{R^2\xi}\boldsymbol{I} + \left(\frac{J_0(R\xi)}{\xi} - \frac{2J_1(R\xi)}{R\xi^2}\right)\frac{\boldsymbol{\xi}\otimes\boldsymbol{\xi}}{\xi R}\right]. \tag{A.5}$$

Using the same technique to evaluate δ_Γ associated to the boundary Γ of the circle, we obtain

$$\widehat{\delta_\Gamma}(\boldsymbol{\xi}) = \frac{1}{V}\int_\Gamma \boldsymbol{e}^{-i\boldsymbol{\xi}\boldsymbol{x}} d\boldsymbol{x} = \mathrm{tr}[\widehat{(\boldsymbol{n}\otimes\boldsymbol{n}\delta)}_\Gamma(\boldsymbol{\xi})] = \frac{2\pi R^2}{L^2}\frac{J_0(R\xi)}{R}. \quad \text{(A.6)}$$

In the case where the circle center is located at the coordinate $\boldsymbol{c}$, the form factors given by the previous expressions should be multiplied by the factor $e^{-i\boldsymbol{\xi}\boldsymbol{c}}$.

Appendix A.2. Lines

For a line connecting two points $\boldsymbol{c}^1$ and $\boldsymbol{c}^2$, the form factor admits the following expression

$$\widehat{\delta_\Gamma}(\boldsymbol{\xi}) = \frac{1}{V}\int_\Gamma \boldsymbol{e}^{-i\boldsymbol{\xi}\boldsymbol{x}} d\boldsymbol{x} = \frac{2l}{V} e^{-i\boldsymbol{\xi}\boldsymbol{c}}\mathrm{sinc}(\boldsymbol{\xi}\boldsymbol{l}), \quad \text{(A.7)}$$

and

$$\boldsymbol{c} = \frac{1}{2}(\boldsymbol{c}^1 + \boldsymbol{c}^2), \quad \boldsymbol{l} = \frac{1}{2}(\boldsymbol{c}^2 - \boldsymbol{c}^1). \quad \text{(A.8)}$$

Since the normal vector is constant on the line, we have

$$\widehat{\boldsymbol{n}\delta_\Gamma}(\boldsymbol{\xi}) = \boldsymbol{n}\widehat{\delta_\Gamma}(\boldsymbol{\xi}), \quad \widehat{\boldsymbol{n}\otimes\boldsymbol{n}\delta_\Gamma}(\boldsymbol{\xi}) = \boldsymbol{n}\otimes\boldsymbol{n}\widehat{\delta_\Gamma}(\boldsymbol{\xi}). \quad \text{(A.9)}$$

Appendix B. Analytical solutions for a stratified material with Kapitza interface

We consider a composite material with an inclusion of dimension $2h \times L$, conductivity k_i at the center of unit cell $L \times L$. The matrix material has the conductivity k_m and the Kapitza interface coefficient is k_s. The material is subject to a macroscopic gradient $E_1 = 1, E_2 = 0$ along direction x. The

gradient in each phase is constant and equal to

$$e_1(x) = e_1^i = \frac{\frac{L}{k_i}E_1}{\frac{2h}{k_i} + \frac{L-2h}{k_m} + \frac{2}{k_s}}, \quad 0 < x < h.$$
$$e_1(x) = e_1^m = \frac{\frac{L}{k_m}E_1}{\frac{2h}{k_i} + \frac{L-2h}{k_m} + \frac{2}{k_s}}, \quad h < x < L/2. \tag{B.1}$$

The temperature jump at the interface has the form

$$\theta^m(h) - \theta^i(h) = \frac{\frac{L}{k_s}E_1}{\frac{2h}{k_i} + \frac{L-2h}{k_m} + \frac{2}{k_s}}. \tag{B.2}$$

and the temperature in each phase is

$$\theta = \theta^i = \left[\frac{\frac{L}{k_i}}{\frac{2h}{k_i} + \frac{L-2h}{k_m} + \frac{2}{k_s}} - 1\right] E_1 x, \quad 0 < x < h$$
$$\theta = \theta^m = \left[\frac{\frac{L}{k_m}}{\frac{2h}{k_i} + \frac{L-2h}{k_m} + \frac{2}{k_s}} - 1\right] E_1 (x - L/2), \quad h < x < L/2 \tag{B.3}$$

Appendix C. Finite Element Models for circular inclusion problem

The circular inclusion of radius $R = 0.3$ [m] is located at the center of the unit cell of size 1 [m]. Due to the symmetry of the problem, only 1/4 of the model limited by the inequality $0 \le x, y \le 0.5$ [m] is considered. For boundary conditions, zero normal flux $j_n = 0$ [W/m^2] on the axis of symmetry $y = 0$ [K] and the upper boundary. Zero physical temperature $T = 0$ [K] (or $\theta = 0$ [K]) is prescribed on the axis of symmetry y and $T = -0.5$ [K] (or $\theta = 0$ [K]) on the right boundary. The conductivities of inclusion and matrix are k_i and k_m and the Kapitza interface coefficient is k_s. The mesh of the model is given in Fig. C.13 composed of 2074 linear triangular elements.

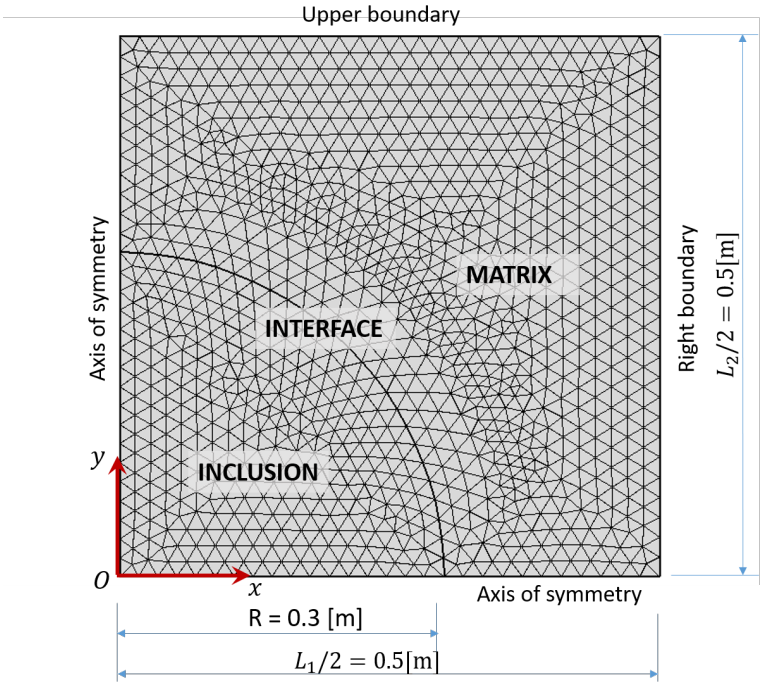

Figure C.13: Finite Element Model for the circular inclusion problem.

References

Bonnet, M., 1999. Boundary integral equation methods for solids and fluids. Wiley.

Brisard, S., Dormieux, L., 2010. FFT-based methods for the mechanics of composites: A general variational framework. Comput. Mater. Sci. 49, 663–671.

Brown Jr, W.F., 1955. Solid mixture permittivities. J. Chem. Phys. 23, 1514–1517.

Eyre, D.J., Milton, G.W., 1999. A fast numerical scheme for computing the response of composites using grid refinement. Eur. Phys. J. Appl. Phys. 6, 41–47.

Greengard, L., Moura, M., 1994. On the numerical evaluation of electrostatic fields in composite materials. Acta numerica 3, 379–410.

Kabel, M., Böhlke, T., Schneider, M., 2014. Efficient fixed point and Newton–Krylov solvers for FFT-based homogenization of elasticity at large deformations. Comput. Mech. 54, 1497–1514.

Kröner, E., 1977. Bounds for effective elastic moduli of disordered materials. J. Mech. Phys. Solids 25, 137–155.

Lucarini, S., Cobian, L., Voitus, A., Segurado, J., 2022. Adaptation and validation of FFT methods for homogenization of lattice based materials. Comput. Meth. Appl. Mech. Eng. 388, 114223.

Michel, J., Moulinec, H., Suquet, P., 1999. Effective properties of composite materials with periodic microstructure: a computational approach. Comput. Method Appl. Mech. Eng. 172, 109–143.

Michel, J., Moulinec, H., Suquet, P., 2000. A computational method based on augmented Lagrangians and fast Fourier transforms for composites with high contrast. CMES(Computer Modelling in Engineering & Sciences) 1, 79–88.

Michel, J., Moulinec, H., Suquet, P., 2001. A computational scheme for linear and non-linear composites with arbitrary phase contrast. Int. J. Numer. Meth. Eng. 52, 139–160.

Monchiet, V., 2018. FFT based iterative schemes for composites conductors with non-overlapping fibers and Kapitza interface resistance. Int. J. Solids Struct. 135, 14–25.

Monchiet, V., Bonnet, G., 2012. A polarization-based FFT iterative scheme for computing the effective properties of elastic composites with arbitrary contrast. Int. J. Numer. Meth. Eng. 89, 1419–1436.

Moulinec, H., Silva, F., 2014. Comparison of three accelerated FFT-based schemes for computing the mechanical response of composite materials. Int. J. Numer. Meth. Eng. 97, 960–985.

Moulinec, H., Suquet, P., 1994. A fast numerical method for computing the linear and nonlinear mechanical properties of composites. C. R. Acad. Sci 318, 1417–1423.

Schneider, M., 2019. On the Barzilai-Borwein basic scheme in FFT-based computational homogenization. Int. J. Numer. Meth. Eng. , 482–494.

Schneider, M., 2020. Lippmann-Schwinger solvers for the computational homogenization of materials with pores. Int. J. Numer. Meth. Eng. 121, 5017–5041.

Taylor, M., 2001. The Dirichlet-Jordan test and multidimensional extensions. Proc. Am. Math. Soc. 129, 1031–1035.

To, Q.D., Bonnet, G., 2020. FFT based numerical homogenization method for porous conductive materials. Comput. Meth. Appl.Mech. Eng. 368, 113160.

To, Q.D., Bonnet, G., 2023a. Fourier transform approach to homogenization of frequency-dependent heat transfer in porous media. Int. J. Numer. Methods Heat Fluid Flow 33, 2023–2048.

To, Q.D., Bonnet, G., 2023b. Fourier transform approach to numerical homogenization of periodic media containing sharp insulating and superconductive cracks. Comput. Meth. Appl. Mech. Eng. 403, 115710.

To, Q.D., Bonnet, G., Nguyen, T.T., 2021. Fourier transform approach to non periodic boundary value problems in porous conductive media. Int. J. Numer. Methods Eng. 122, 4864–4885.

Vondřejc, J., Zeman, J., Marek, I., 2014. An FFT-based Galerkin method for homogenization of periodic media. Comput. Math. Appl. 68, 156–173.

Willot, F., Abdallah, B., Pellegrini, Y.P., 2014. Fourier-based schemes with modified Green operator for computing the electrical response of heterogeneous media with accurate local fields. Int. J. Numer. Meth. Eng. 98, 518–533.

Zeman, J., Vondrejc, J., Novak, J., Marek, I., 2010. Accelerating a FFT-based solver for numerical homogenization of periodic media by conjugate gradients. J. Comput. Phys , 8065–8071.